HHS Public Access

Author manuscript

Small Methods. Author manuscript; available in PMC 2023 January 01.

Published in final edited form as:

Small Methods. 2022 January ; 6(1): e2100900. doi:10.1002/smtd.202100900.

Epidermis-inspired Wearable Piezoresistive Pressure Sensors using Reduced Graphene Oxide Self-Wrapped Copper Nanowire Networks

Yangzhi Zhu[#,*],
Terasaki Institute for Biomedical Innovation, Los Angeles, California 90064, United States

Martin C. Hartel[#],
Terasaki Institute for Biomedical Innovation, Los Angeles, California 90064, United States; Department of Biomedical Engineering, University of California, Los Angeles, Los Angeles, California 90095, United States

Ning Yu,
Department of Chemical and Environmental Engineering, Bourns College of Engineering, University of California, Riverside, Riverside, California 92521, United States

Pamela Rosario Garrido,
Terasaki Institute for Biomedical Innovation, Los Angeles, California 90064, United States; Department of Electric and Electronic Engineering, Technological Institute of Merida, Merida, Yucatan 97118, Mexico

Sanggon Kim,
Department of Chemical and Environmental Engineering, Bourns College of Engineering, University of California, Riverside, Riverside, California 92521, United States

Junmin Lee,
Terasaki Institute for Biomedical Innovation, Los Angeles, California 90064, United States

Praveen Bandaru,
Terasaki Institute for Biomedical Innovation, Los Angeles, California 90064, United States

Shenghan Guan,
Terasaki Institute for Biomedical Innovation, Los Angeles, California 90064, United States

Haisong Lin,
Terasaki Institute for Biomedical Innovation, Los Angeles, California 90064, United States; Department of Biomedical Engineering, University of California, Los Angeles, Los Angeles, California 90095, United States

[*]Corresponding Authors: yzhu@terasaki.org (Y. Zhu); rxyan@engr.ucr.edu (R. Yan); khademhosseini@terasaki.org (A. Khademhosseini).
[#]Equal contribution

Supporting Information
Supporting Information is available from the Wiley Online Library or the author.

Conflict of Interest
The authors declare no conflict of interest.

Sam Emaminejad,
Terasaki Institute for Biomedical Innovation, Los Angeles, California 90064, United States; Department of Biomedical Engineering, University of California, Los Angeles, Los Angeles, California 90095, United States

Natan Roberto de Barros,
Terasaki Institute for Biomedical Innovation, Los Angeles, California 90064, United States

Samad Ahadian,
Terasaki Institute for Biomedical Innovation, Los Angeles, California 90064, United States

Han-Jun Kim,
Terasaki Institute for Biomedical Innovation, Los Angeles, California 90064, United States

Wujin Sun,
Terasaki Institute for Biomedical Innovation, Los Angeles, California 90064, United States

Vadim Jucaud,
Terasaki Institute for Biomedical Innovation, Los Angeles, California 90064, United States

Mehmet R. Dokmeci,
Terasaki Institute for Biomedical Innovation, Los Angeles, California 90064, United States

Paul S. Weiss,
Department of Biomedical Engineering, University of California, Los Angeles, Los Angeles, California 90095, United States; Department of Chemistry & Biochemistry, Department of Materials Science & Engineering, and California NanoSystems Institute, University of California, Los Angeles, Los Angeles, California 90095, United States

Ruoxue Yan*,
Department of Chemical and Environmental Engineering, Bourns College of Engineering, University of California, Riverside, Riverside, California 92521, United States; Materials Science & Engineering Program, Bourns College of Engineering, University of California, Riverside, Riverside, California 92521, United States

Ali Khademhosseini*
Terasaki Institute for Biomedical Innovation, Los Angeles, California 90064, United States

Abstract

Wearable piezoresistive sensors are being developed as electronic skins (e-skin) for broad applications in human physiological monitoring and soft robotics. Tactile sensors with sufficient sensitivities, durability, and large dynamic ranges are required to replicate this critical component of the somatosensory system. Multiple micro/nano-structures, materials, and sensing modalities have been reported to address this need. However, a trade-off arises between device performance and device complexity. Inspired by the microstructure of the spinosum at the dermo epidermal junction in skin, we developed a low-cost, scalable, and high-performance piezoresistive sensor with high sensitivity (0.144 kPa^{-1}), extensive sensing range (100 Pa -15 kPa), fast response time (less than 150 ms), and excellent long-term stability (over 1000 cycles). Furthermore, the piezoresistive functionality of the device was realized via a flexible transparent electrode (FTE) using a highly stable reduced graphene oxide self-wrapped copper nanowire (CurGONW)

network. The developed nanowire-based spinosum microstructured FTEs are amenable to wearable electronics applications.

Graphical Abstract

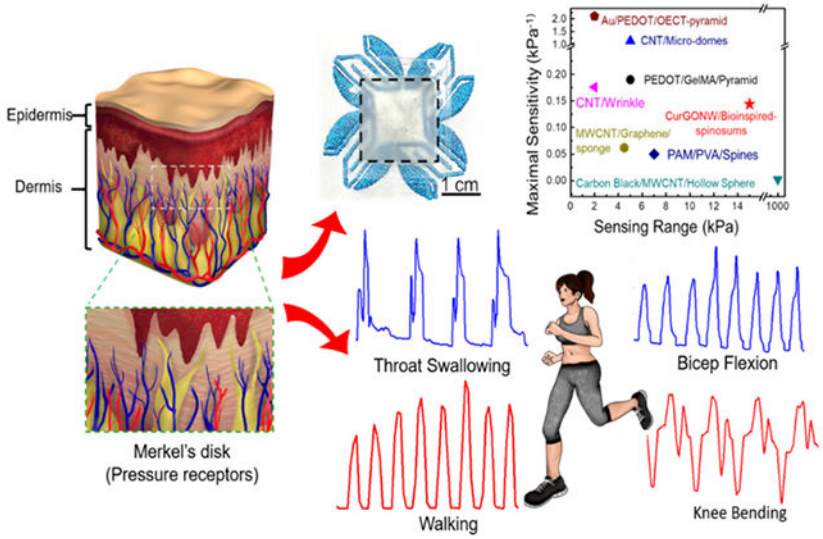

Keywords

wearable electronics; electronic skin; piezoresistive sensor; bioinspired microstructure; flexible transparent electrode; core-shell nanowires

1. Introduction

The human skin is the body's largest organ, responsible for critical functions including tactile sensing, temperature sensing/regulation, and barrier properties.[1] Electronic skin (E-skin) ultimately seeks to recreate these functions for prosthetics and soft robotics applications to improve human-robot interactions.[2-8] In either application, a primary challenge lies in creating wearable diagnostic and monitoring devices that can maintain high sensitivity and durability over the wide range of pressures experienced by the human skin. Regardless of the mode of operation (i.e., piezoresistive, capacitive, piezoelectric), most pressure sensors are comprised of two key components. The first is a microstructure that can readily localize stress concentrations, and the second is an electrically conductive material that can transduce this stress into a quantifiable signal. Multiple microstructures (e.g., microdomes[9-11], micropyramids[12-14] and micropillars[15-17]) and nanomaterials (e.g., metals[18-20] and carbon nanotubes (CNTs)[10, 21, 22]) have been reported to impart pressure sensors with favorable sensitivities over large ranges.[23] However, most devices require complex microfabrication techniques (i.e., lithography and etching) to generate periodic microstructures, and rely on costly materials like gold, silver, and CNTs to functionalize those surfaces. Thus, we modified a cost-effective and scalable approach from a materials and device perspective to fabricate high-quality and robust wearable pressure sensors.

The successive progress of nanomaterial synthesis and related device fabrication has ushered in many achievements in actuator/robotic devices,[24-27] energy storage devices,[28-30] biosensor devices,[31-34] flexible displays,[35, 36] and human-machine interfaces.[37, 38] Several notable nanomaterials such as graphene,[39, 40] metal nanoparticles (particularly liquid metal),[41-43] conductive polymers,[44, 45] and metal nanowires/nanofibers[46, 47] have been extensively exploited for developing next-generation wearable electronic devices. Metal nanowires have garnered significant attention among these candidate materials because of their excellent electrical, mechanical, and optical properties. Such characteristics have encouraged their use in recent flexible devices, including e-skin,[35, 48, 49] wearable thermoregulators,[50-52] smart windows,[53-55] and FTEs[56-58] to replace traditional indium tin oxide (ITO) films. Among the various kinds of metal nanowires, copper nanowires (CuNWs) are promising due to their low cost without compromising on electrical, thermal, and optical properties. However, a daunting obstacle for the device-level commercialization of CuNWs is their vulnerability to oxidation under ambient environments.[59] To leverage the benefits of CuNWs while improving their long-term stability for device-level applications, we modified a recent method developed by Dou et al. and coated reduced graphene oxide (rGO) on the surfaces of CuNWs.[60] The CurGONWs were imparted with improved electrical stability compared to pristine CuNWs.

When deciding which microstructure to functionalize with the synthesized CurGONWs, we were inspired by the geometry of the spinosum in the epidermis to fabricate wearable sensors using commercially available sandpaper as a template. This work demonstrates a solution-processed technique to synthesize CurGONWs with enhanced chemical stability for FTEs. GO nanosheets with controllable thicknesses ranging from *ca*. 3 nm to 12 nm were self-assembled on the CuNW surfaces uniformly and conformally. The CurGONWs are significantly stable under ambient conditions, even in high temperature and high humidity environments. We first developed durable, flexible CurGONW-FTEs with comparable ITO-level performance as a proof-of-concept. Finally, we demonstrated a robust and flexible epidermis-bioinspired spinosum microstructured piezoresistive sensor with Cu-rGO core-shell NWs (CurGONW-SMPS) capable of human physiological monitoring for wearable electronics and soft robotic applications.

2. Results and Discussion

2.1. Fabrication and Mechanism Revelation of CurGONW-SMPS

Nature often offers inspiration to advance science and engineering, particularly when studying microstructures and their uses for bioinspired electronic devices. For instance, skin is a critical sensory organ that transduces surrounding environmental cues, including humidity, pressure, and temperature. Specifically, the microstructured spinosum located at the dermo epidermal junciton is composed of Merkel disks as pressure receptors for mechanotransduction of sensitive touch, as shown in Figure 1a. Since the spinosum geometry can generate sharp and regional stress concentrations at the peaks near these tactile receptors, it plays a significant role in sensory stimuli for improved pressure discrimination.[61] Furthermore, compared to other commonly used surface microstructures (pyramid, hemisphere, and cylinder), theoretical simulations of pressure distribution have verified that

spinosum microstructured devices yield favorable sensitivities and linear ranges.[61] As shown in Figure 1b, the microscopic morphology of the spinosum has a similar surface structure to that of sandpaper. The morphology of the micropatterned substrate shows smooth interconnected ridges and dispersive holes, indicating a high density of spinosum microstructures. Bioinspired by this unique structure, we used sandpaper as a template to fabricate spinosum microstructured surfaces with a random roughness (Figure 1c). Figure 1d depicts the overall device fabrication process of the epidermis-bioinspired CurGONW-SMPS. The polydimethylsiloxane (PDMS) was cast onto sandpaper to imprint a spinosum microstructure on this flexible substrate. Oxygen plasma was applied to treat the surface to increase its hydrophilicity; thereby guaranteeing a uniform large-area NW network. After spray coating the highly conductive CurGONW suspension, thermal annealing was applied to evaporate the remaining solvent and enhance the adhesion between NWs and the flexible substrate. These fabrication techniques, namely template molding and spray coating, are much more amenable to scalable production than comparable cleanroom approaches. Commercial spray-coating systems and vacuum ovens could be employed to streamline the PDMS molding, curing, and NW functionalization for more high throughput device fabrication compared to traditional wafer-scale techniques. Furthermore, devices with different shapes and sizes could be cut from the functionalized PDMS to be tailored for specific applications such as soft robotics and wearable sensors.

Finally, wire bonding and face-to-face packaging were conducted to complete the bioinspired CurGONW-SMPS. The optical image of the final device is shown in Figure 1e. The working mechanisms of the CurGONW-SMPS are summarized in Figure 1f. Initially, under no external pressure, there are few contact points between the two spinosum microstructured FTE with CurGONWs. A rapid increase in the contact area between the spinosum microstructured FTEs can measurably enhance new NW connections with subtle applied pressure. With increased applied pressure, the overlapping NWs continue to decrease the measured resistance. As a result, few new NW connections are made in the high-pressure regime, resulting in a saturated electrical response until the sensor returns to its initial state upon unloading.

2.2. Synthesis and Characterization of CurGONW-SMPS

We report a facile solution-processed CurGONW synthesis recipe to functionalize the bioinspired spinosum microstructures. Figure 1g-k depict the overall strategy for synthesizing GO self-wrapped CuNWs (CuGONWs). First, the GO nanosheets were prepared using the modified Hammer method and confirmed with UV-Vis spectra, transmission electron microscopy (TEM), and X-ray powder diffraction (XRD) (Figure S1, Figure 2j). The GO was then well-dispersed in a methanol solution for subsequent reactions. The as-synthesized CuNWs were then added to the GO solution to form a homogeneous mixture dispersion. The self-wrapping process occurs quickly in organic solvents (methanol) under mild ultrasonication, and the GOCuNW samples were obtained after centrifugation and purification. Few nanometer-thick oxide layers (CuO, Cu_2O) were found on the CuNW surface, as confirmed by high-resolution transmission electron microscopy (HRTEM) images (Figure S2). It is believed that these oxide layers interact strongly with the many carboxyl and hydroxyl functional groups present in heavily oxidized GO, which effectively

bridges the copper oxide surface on the CuNWs.[60] Therefore, they provide a vital driving force for the spontaneous wrapping of GO on CuNW surfaces.

Figure 2 displays the morphological characterization of the CuGONWs using various measurement techniques. The as-synthesized high-purity CuGONW samples were confirmed by scanning electron microscopy (SEM) images in Figure 2a. Figure 2b and Figure S3 show typical HRTEM images of an individual CuGONW. A 3 nm-thick GO nanolayer was uniformly coated on the CuNW surface. A magnified TEM image (Figure 2c) demonstrates the prominent interfacial layer between the GO and crystalline Cu.

Moreover, energy-dispersive X-ray spectroscopy (EDS) mapping on an individual CuGONW verified the well-defined core-shell morphology. As validated in Figure 2d-g, the NW core was comprised of Cu (green color), while oxygen (blue) and carbon (red) formed a conformal and consistent shell on the edge of the nanowire. Figure 2h shows the GO nanosheet solutions and the CuNW samples before and after GO coating. The X-ray diffraction analysis (XRD) spectra confirm the existence of Cu_2O and GO (Figure 2i-j), which supports the hypothesis that the thin oxide at the CuNW surface interacts strongly with the hydroxyl and carboxyl groups from the graphene oxide layer. Furthermore, Figure 2k displays the Raman spectra of pristine CuNWs (green) and CuGONWs (blue) measured with an excitation wavelength of 532 nm. The CuGONW spectrum shows typical D and G bands of GO at *ca.* 1356 cm^{-1} and 1604 cm^{-1}, consistent with their published values.[62, 63]

In addition to facile core-shell NW synthesis, this approach enables tunable GO coating thickness by controlling the reaction time. The corresponding transmission electron microscope (TEM) images of the CuGONW synthesized with increasing reaction time showed an increasing coating thickness of *ca.* 3 nm, 6 nm, and 12 nm, respectively (Figure S3). The measured thickness was based on the contrast between the Cu core and GO shell in the TEM images.

2.3. Fabrication and Characterization of CurGONW-FTE

After characterizing the as-synthesized CuGONW, we constructed flexible CuGONW-FTEs via our previous vacuum filtration protocol,[68] as shown in Figure S4. First, a dilute CuGONW suspension was transferred onto a nitrocellulose filter membrane via vacuum filtration. Next, the NW network was transferred to a flexible substrate (poly(ethylene terephthalate), or PDMS) by applying pressure to the backside of the filter. Then, the FTEs were annealed using forming gas to reduce the GO and copper oxides while creating junction-free contacts where the nanowires overlap. Figure S5 depicts a schematic overview of the thermal reduction process.

To optimize the conductivity of the CuGONWs after thermal reduction, we then annealed the FTEs under different temperatures, as shown in Figure S6. A decrease in the sheet resistance was observed when the annealing temperature was increased to 280 °C because GO was gradually thermal reduced. This significant improvement in the electrical performance of the CurGONW-FTEs is attributed to the removal of the copper nanowire oxides and the thermal reduction of the GO nanoshells, as characterized by the XRD

measurement summarized in Figure S7. The copper oxide peaks disappeared, and the GO nanoshells were reduced. However, at higher temperatures (>320 °C), the CurGONWs underwent permanent damage resulting in a dramatically increased sheet resistance. Figure S8 summarizes SEM images of the CurGONW-FTEs annealed at varying temperatures. The CurGONW morphology was well preserved to around 280 °C or lower. At 320 °C, some wires started to melt, and more NW disconnections were found. Finally, all the NW networks were destroyed and lost electrical function at 360 °C. Therefore, the optimized annealing temperature of the CurGONW-FTEs was observed to be around 280 °C. Additionally, at this temperature, the graphene oxide nanosheets were thermally reduced to rGO, as seen visually by the sample's color change and XRD characterization (Figure S9). The XRD diffraction peak shifted from *ca.* 11° to 24°, suggesting that the π-π stacking distance decreased from 0.80 nm to 0.37 nm due to the removal of C=O and OH groups on the GO layer. Furthermore, the Raman spectra further confirmed the transition of GO to rGO (Figure 2j, **top**). I_D/I_G decreased after the CuGONW sample was annealed in forming gas under 280 °C for one hour, indicating substantial recovery of the conjugated graphitic framework after removing oxygen functional groups. We then investigated the optical/electrical performance of the CurGONW-FTEs with different rGO coating thicknesses, as displayed in Figure 3e. The resultant CurGONW-FTEs yielded slightly improved electrical performance with comparable optical transmission to pristine CuNW-based flexible transparent electrodes (CuNW-FTEs). This improvement can be attributed to several factors: first, the GO nanoshell could be effectively reduced to rGO, and thermal annealing created "junction-free" connections between NWs (Figure S10). Secondly, the NW network could be uniformly dispersed in the colloidal suspension, which encouraged more uniform electrode coatings, further improving the charge transfer between NWs.

To continue device characterization, we prepared CurGONW-FTEs with different NW loading amounts. As a result, they yielded sheet resistances of 4.6 Ω/sq, 9.8 Ω/sq, 28.4 Ω/sq, 50.8 Ω/sq at different transparency of 80%, 85%, 90%, and 95%, respectively, all of which were achieved under a 550 nm wavelength shown in Figure 3a, which was comparable to silver nanowire-based FTEs and commercial ITO (Figure 3b).

The long-term stability of the NW-based FTEs under ambient conditions was also investigated, as shown in Figure 3c. The pristine CuNW-FTEs exhibited weak stability with their electrical properties decaying within a few hours at 80 °C in a 100% humid environment (Figure 3d). However, the CurGONW-FTEs retained much better stability without any noticeable degradation because of the sufficient protection endowed by the rGO nanoshells. The sheet resistance of CurGONW-FTEs was almost identical to that of fresh CuNW-FTEs over 320 days of storage in the air. For comparison, the original CuNW-FTEs were severely degraded after one month of being exposed to air. In addition, the CurGONW-FTEs showed enhanced performance compared with CuNW-FTEs in terms of transparency and sheet resistance (Figure 3e). The sheet resistance of CurGONW-FTEs (3 nm- and 6 nm-thick rGO layer) displayed better conductivity than the uncoated CuNW-FTEs. These superior properties are attributed to several improvements. First, the thin rGO coating improves the junction and electrical conduction from nanowire to nanowire. We measured

the junction resistance of two overlapped CuNWs and CurGONWs, shown in Figure S11. The NW was picked up using our previously reported method[69] to fill the gap between two separate gold electrodes. According to the results, the junction resistance decreased significantly with a thin rGO coating on the nanowire surface. Like the graphene-coated CuNWs,[70] the rGO coating also improves the electrical conductivity of the NW-NW junctions, which is the main contributor to the sheet resistance of CurGONW-FTEs.[71] Second, the CurGONWs form a more homogeneous dispersion, resulting in less aggregation than pristine CuNW samples. This translates to fewer aggregated clumps during membrane filtration compared to the pristine CuNW samples.

Device flexibility represents another critical factor for ensuring the use of FTEs in wearable applications. Therefore, we further investigated how stretching and bending cycles would affect the electrical resistance of the CurGONW-FTEs. The stretching and bending tests were carried out using a simple setup constructed in-house that utilizes a syringe pump to produce repetitive motion. The electrical conductivity yields a tiny increase up to a bending radius of 1 mm, which could be recovered upon release (Figure 3f). Moreover, the electrical performance did not show evident deterioration even after 1000 cycles of inner bending and outer bending with a 5 mm-bending radius (Figure 3g). Such results verify the superior electromechanical stability of the CurGONW-FTEs. We then investigated the sheet resistance change to respond to tensile strain change at a maximal strain of 600% (Figure 3h). Similar to the bending test results, the sheet resistance of the CurGONW-FTEs increased during stretching. However, it could almost be entirely recovered to its original state when the strain was released. This result can be attributed to the fact that metal nanowires are the ideal material candidate for stretchable transparent electrodes as copper itself is one of the most ductile metals that can easily tolerate tensile stress and deformation. In addition, the copper nanowire percolation network can effectively tolerate deformation without a significant decay in conductivity.[58, 72] Furthermore, our customized PDMS substrate has good stretchability, as much as 600%, that can accommodate the extra stress during the stretching cycles. As shown in Figure 3h, with the increased strain the CurGONW network structures themselves started to slightly deform and partly ruptured with the increased strain. However, the nanowire percolation networks were still moderately good to yield robust high conductivity. Regarding the strain impact optical property, the thin diameter and long length of the nanowires would, in principle, boost light transmission while maintaining high conductance.[73, 74] Also, the facile aqueous-processed strategy can result in high quality, well-dispersed nanowire networks, which can also allow light transmission. All of these features ensure good optical performance of the as-prepared CurGONW-SMPS, even during stretching/bending cycling tests.

Furthermore, we conducted stretch-release cycling tests to validate their long-term stability (Figure 3i). The electrical resistance of the CurGONW-FTEs only slightly increased with stretching even after 1000 cycles, which might be attributed to the high tensile property of the NW network. The above features suggest several advantages for using CurGONW-FTEs in high-performance wearable electronics.

2.4. Mechanical and Electrical Characterization of CurGONW-SMPS

We then investigated the mechanical properties of the assembled SMPS as they represent a critical parameter for using pressure sensors in practical applications. The fabricated pressure sensor's mechanical hysteresis was characterized using cyclic compression tests at varying compression stresses (1, 3, 8, and 10 kPa) with a 1 mm/min compression rate. As illustrated in Figure 4a-b, the compressive stress could almost be fully recovered at all the tested values upon releasing the applied load. A tiny residual strain might be generated at higher pressures due to permanent deformations such as cracks and wrinkles. Furthermore, the device's mechanical stability at varying compression rates was investigated. An invariable pressure of 1000 Pa was repeatedly applied/unloaded to the sensor at varied compression speeds (0.5, 0.8, 1.0, 3.0, 5.0 mm/min) in Figure 4c. The overlapping waveforms without y-axis separation and with the reported R/Ro values can be found in Figure S12. The high elasticity and fast response time of our device resulted in a resistance output whose magnitude remained unaffected by the varying compression rates. These results confirm that the bioinspired CurGONW-SMPS maintains good reliability, encouraging their application for detecting various motions.

Despite some elastic deformation within the PDMS substrate, which leads to a particular response time delay, the sensor yields a response and recovery time of less than 150 ms (Figure 4d), which is enough to satisfy the requirements for real-time motion monitoring. Figure 4e shows the *I-V* current response when applying -4 to 4 V for the bioinspired CurGONW-SMPS using 800 grit sandpaper as the template. The linear dependence of voltage on current under varying pressures verifies that the bioinspired piezoresistive sensor obeys Ohm's law. In addition, the increasing slope of the *I-V* curves as the applied pressure increases suggests a related decrease in the resistance of the device.

The piezoresistive sensor's sensitivity is an essential parameter for assessing device performance and was characterized using the following equation:

$$S = \frac{\Delta R \,/\, R_0}{\Delta P}$$

Where ΔR, R_0, and ΔP denote the resistance change before and after loading, the unloaded resistance, and the applied pressure change, respectively.

We then investigated how NW loading density and surface microstructure roughness would affect the sensitivity of the pressure sensor. First, we fabricated devices with varying NW loading concentrations to characterize how the device's initial conductivity affected its overall performance. The $\Delta R/R_0$ versus pressure change for this CurGONW-SMPS with varied NW loadings concentrations are summarized in Figure 4f and Figure S13. The results show that using moderate NW concentrations exhibits the maximum sensitivity compared to sensors made with other NW concentrations (low, high, very high). When the NW loading was low, insufficient conductive pathways could be formed even under applied stress. When the NW loading was too high, only subtle conductivity changes were observed by loading pressure as there were already high numbers of conductive routes available in the unloaded state. We then fabricated CurGONW-SMPS with fixed medium NW loading concentrations

and varied the microstructure roughness. Figure 4g shows the $\Delta R/R_0$ versus ΔP of the CurGONW-SMPS assembled with several degrees of sandpaper roughness (400, 600, 800, 1000). For the most sensitive case using the 800 grit as a template, the $\Delta R/R_0$ decreased sharply below 1 kPa, then decrease mildly by a certain amount between 1 and 5 kPa and decrease relatively slowly, ranging from 5 and 15 kPa. The corresponding sensitivities are 0.144 kPa^{-1}, 0.027 kPa^{-1}, and 0.004 kPa^{-1}, respectively. The overall trend of the four roughness conditions might be attributed to the fact that when the roughness is too large, even the compressed microstructures cannot effectively increase the number of conductive channels, and sensing small stresses is extremely difficult. The density of spinosum microstructures was significantly increased as the roughness was reduced. Therefore, tiny pressure changes could effectively increase the number of conductive channels in a large area, ensuring improved device sensitivity. When the microstructure density was too large (1000 grit), the device's performance was likely reduced because too many NW connections could be made even in the unloaded state. To test this hypothesis and to elucidate how microstructure morphology impacts sensor performance, we utilized 3D optical surface profilometer to image our PDMS electrodes (Figure S14). As expected, with increasing grit size (from 400 to 1000) the average roughness (Ra), root mean squared roughness (Rq), and maximum surface height (Rt) all show a decreasing trend. The highest reported sensitivity of 0.144 kPa^{-1} (for 800 grit) yielded the following values: Ra=5.70μm, Rq=7.40μm, Rt =57.42μm and were quite similar to those for the 600 grit PDMS (Ra=5.89 μm, Rq=7.66μm, Rt=59.23μm) which can explain their similar sensing performance. Once the surface is too rough (400 grit) or too smooth (1000 grit) the sensitivity is drastically reduced, indicating their surface roughness parameters are beyond the optimal range for such nanowire-based piezoresistive sensors.

Figure 4h demonstrates the change in normalized resistance of the 800-grit bioinspired spinosum microstructured piezoresistive sensor with CurGONWs during step compressions under varying pressures from 0 to 15 kPa with a 30 s holding time. As previously explained, the resistance gradually decreases with increased applied pressure because of increased conductive pathways. Furthermore, no obvious drift or hysteresis in the resistance was observed during the holding time, indicating the favorable stability of our CurGONW-SMPS compared to other piezoresistive sensors. Figure 4i and Table S1 compare the sensitivity performance of our sensor with other recently published works spanning various microstructures, nanomaterials, and sensing modalities (capacitive and piezoresistive). Furthermore, as demonstrated previously, the sensitivity and linear range can be easily tuned for specific applications by varying both NW loading concentration and microstructure roughness. While recent works using bulk graphene oxide have achieved notable improvements toward ultra-high sensitivities (>100kPa^{-1})[81] and large sensitive ranges (>100kPa),[82] this approach leads to several disadvantages. Namely, they require substantially more raw materials (GO) than our NW approach and result in a near total lack of transparency, both of which are important considerations for the successful commercialization of unobtrusive wearable devices.

Moreover, to better characterize the stability and durability of the bioinspired CurGONW-SMPS, 1000 cyclic pressure cycles of 15 kPa were applied to the sensor. As depicted in Figure 4j, the normalized resistance remains virtually unchanged. The figure inset confirms

that the resistance waveform is almost identical to its initial response, even after 1000 cycles. Furthermore, the calculated resistance change drops only 3%, verifying that the sensor possesses superior stability and durability. These favorable electromechanical properties are attributed to the robustness of the applied NW network and the excellent elastic properties of the microstructured substrate.

2.5. Real-time Monitoring of Human Physiological Activities

Given that these bioinspired CurGONW-SMPSs possess excellent stability, fast response times, and sufficient sensitivity, we investigated their performance in real-time human monitoring applications. By using transparent adhesive bandages, the CurGONW-SMPS could be intimately attached to various body locations. Figure 5a-c shows the real-time conductance changes of different physical signals, namely bicep flexion, wrist flexion, and neck torsion, were successfully realized. The motion states are readily distinguishable by comparing the shape and intensities of the graphs. Moreover, the bioinspired CurGONW-SMPS can recognize distinct swallowing actions and the carotid arterial pulse when placed above the larynx and centered on the carotid artery, respectively (Figure 5d,e, S15, and S16). The average beats per minute (BPM) could be calculated by measuring the time delay between pulse peaks, which yielded a value of 80 BPM and was consistent with the Apple Watch Series 3 value of 79 BPM.

Furthermore, two features of the carotid pulse, augmentation index (AIx, defined as augmented pressure/pulse pressure) and time to the first systolic inflection (T1), could be extracted. The average carotid AIx and T1 values were 25% and 100 ms, respectively, within the reported average values for a healthy volunteer.[83] The CurGONW-SMPS could also detect other bodily motions for soft robotic applications, such as finger pressing strength and time interval, quick tapping and bending, the bending-releasing motion of the knee, and even walking (Figure 5f-j). Their corresponding curves also confirm minimal signal drift as the conductance values are practically unchanged following repetitive motions. Certain baseline and peak signal differences over repeated movements such as bicep flexing are attributed to the natural variations of the human subject’s ability to replicate the exact degree of motion. In future works, advanced signal feature extraction algorithms will be implemented to parse out important features and exclude confounding ones. Nonetheless, these CurGONW-SMPSs can be used for electronic skin applications due to their excellent flexibility, sensitivity, stability, and quick response time.

3. Conclusion

In summary, bioinspired by the geometry of the spinosum at the dermo epidermal junction, we developed a scalable and low-cost microstructured piezoresistive sensor with CurGONWs. The sensors enabled real-time monitoring of human motions and subtle physiological signals for personalized healthcare applications. Both high sensitivity and broad sensitive range were achieved because of the bioinspired spinosum microstructures.

The sensor’s electrical functionality was imbued using a solution-processed approach to prepare CurGONWs with controllable rGO coating thicknesses. High-quality FTEs were fabricated via a vacuum filtration method and displayed excellent electrical, optical,

and elastic performance. Furthermore, the CurGONWs enabled highly durable FTEs under ambient conditions and high temperature/humidity environments while maintaining comparable performance to commercial ITO to promote the wide accessibility of wearable sensors.

We thus envision that such bioinspired spinosum microstructured FTEs will be broadly used in various wearable electronic applications due to their amenability for scalable production, excellent flexibility, and long-term stability in harsh environments.

4. Experimental Section

Materials:

Graphite, sodium nitrate ($NaNO_3$), concentrated sulfuric acid (H_2SO_4), potassium permanganate ($KMnO_4$), hydrogen chloride (HCl), toluene, and methanol were purchased from Thermo Fisher Scientific (United States). All chemicals were used directly without further purification. Copper nanowires were prepared using our recently developed work. The PDMS (Sylgard 184) elastomer was obtained from Dow Corning (United States). The various sandpaper grits (400, 600, 800, 1000) were purchased from Amazon (United States).

Characterizations:

Scanning electron microscopy images were taken using an FEI NovaNanoSEM450 (United States) scanning electron microscope. Tunneling electron microscopy images were taken using an FEI Tecnai12 Transmission Electron Microscope. UV-Vis-Near (NIR) spectra were measured with Varian Cary 50UV/Vis spectrophotometers. X-ray diffraction spectroscopy was characterized using an Empyrean diffractometer and Cu K_α radiation with an output power of 1.6 kW at a voltage of 40 kV. Raman spectroscopy was carried out directly on a silicon wafer with Horiba LabRam. The 3D surface characterization images were captured using a Wyko NT3300 optical surface profilometer. Each image represents a 1 mm × 1 mm section of the PDMS electrodes templated with varying grits of sandpaper.

GO Synthesis:

Based on the modified hummer method, 1 g graphite (325 mesh) was put to concentrated H_2SO_4 in an ice bath for 10 min under stirring. Then, 3 g $KMnO_4$ was put into the mixture slowly to maintain the suspension temperature no higher than 25 °C. Successively, the reaction system was moved to a water bath which was kept at 40 °C and stirred for almost 4 hours. Then, 50 mL DI water was added, and the mixture solution was stirred at around 95 °C. Another 100 mL DI water was newly added and followed by slow addition of hydrogen peroxide, resulting in the solution's color shifted from dark brown to yellow. Next, the mixture was purified and rinsed with diluted HCl suspension to remove extra metal ion residues. The final solid was dried and diluted to make a graphite oxide suspension. It was purified for six days with a dialysis membrane to eliminate the rest metal residues. The resultant graphite oxide suspension was then sonicated until it was exfoliated to GO and acid. The graphene oxide dispersion was then centrifuged several times to remove the unexfoliated graphite powder.

CuGONW Synthesis:

In a typical synthesis, to wrap a 3 nm thick-GO layer on the CuNW surface, GO nanosheet aqueous solution (0.5 mg/mL, 1 mL) was diluted in 20 mL methanol. Then CuNW toluene solution (1 mg/mL, 2.5 mL) was added while maintaining stirring. The suspension was sonicated for 10 min to produce the CuGONWs. Next, the nanowires were centrifuged at 2000 rpm for 30 min. Then the NWs were rinsed three times with ethanol by centrifugation-redispersion cycles to eliminate extra graphene oxide. Finally. The samples were stored in ethanol for further use. The thickness of the GO nanoshell could be tuned by controlling the mass ratio of the GO nanosheet and CuNW or the reaction time.

CurGONW-FTE Fabrication:

CuGONWs were dispersed in IPA solution and sonicated to yield a homogeneous dispersion to prepare an FTE. Then this nanowire solution was vacuum-filtered onto a polytetrafluoroethylene porous (PTFE) membrane. Then the NWs were transferred onto a PET or PDMS substrate by hand-pressing the backside of the PTFE membrane. Then the CuGONW-FTE was annealed under forming gas at 280 °C for 1 h to reduce GO and copper oxides.

Bioinspired CurGONW-SMPS Fabrication:

Firstly, a mixture of PDMS liquids (ratio of base and curing agent is 10:1) was degassed and then spin-coated at a speed of 200 rpm for 30 s onto 2 cm × 2 cm sections of various grit sandpapers (400, 600, 800, 1000). The PDMS was then cured in an oven at 80 °C for 20 min and carefully peeled off from the sandpaper template. The templated PDMS surface was then activated with oxygen plasma for 2 min to increase their hydrophilicity. Next, the PDMS was immediately placed on a hotplate set to 100 °C while the as-prepared CuGONWs were loaded into a spray gun and applied to the PDMS at around 10 cm distance with 30 kPa driving pressure. The functionalized PDMS electrodes were then baked at 280 °C to reduce the GO and vaporize any remaining solvent. Finally, one wire was bonded to each electrode using silver epoxy, and two electrodes were adhered face-to-face using double-sided tape to create the final piezoresistive sensor device.

Electrical and Mechanical Measurements:

The sheet resistance measurement is modified that was based on Cui's work.[84] First, a glass substrate (Thermo Fischer Scientific) was rinsed with acetone and ethanol at least three times, then 4 nm/100 nm (Cr/Au) was deposited via a custom Angstrom Engineering thermal evaporator system. A nanowire mesh was then separately pressed onto the surface for the creation of the devices. The nanowire mesh was then transferred onto the prepared masks. Finally, the sheet resistance of the electrode was characterized using a Signatone CM200 probe station and Agilent 4155A Semiconductor Parameter Analyzer. All other electrical characterization studies were conducted using an Agilent B2902A source-measure unit under an applied bias of 100 mV controlled by Keysight B2900A Quick IV measurement software. For stretching/bending tests of CurGONW-FTE, a simple setup constructed in-house that utilizes a syringe pump to produce repetitive motion carried out the stretching/bending cycling tests. The syringe pump was controlled by LabView

software. To investigate how mechanical stress influenced the CurGONW-SMPS device's electrical behavior, an Instron (5900 Series) with a force resolution of 11×10^{-4} N was employed to apply pressure and to report stress/strain while the Agilent B2902A reported electrical changes. The force and displacement of the test head were controlled using the Instron Bluehill 3 software. All mechanical tests were operated in compressive stress mode preloaded with 0.01N of force to ensure good contact before applying the pressure profile.

Institutional Review Board Approval for Human Subject Testing:

The conducted human subject experiments were performed in compliance with the protocols that have been approved by the Institutional Review Board (IRB) at the University of California, Los Angeles (IRB#17-000170). All subjects gave written informed consent before participation in the study. For all demonstration on human skin, signed consent was obtained from the volunteer.

Supplementary Material

Refer to Web version on PubMed Central for supplementary material.

Acknowledgments

The authors gratefully acknowledge funding from the National Institutes of Health (CA214411, AR074234, GM126571, TR003148). This work is also supported by the National Science Foundation under Grant No. CHE-1654794. Finally, the authors acknowledge our colleagues from the Terasaki Institute for Biomedical Innovation, the University of California, Los Angeles, and the University of California, Riverside, for helpful discussions.

References

1. Someya T; Amagai M, Nature Biotechnology 2019, 37 (4), 382–388. DOI 10.1038/s41587-019-0079-1.
2. Nature Nanotechnology 2017, 12 (11), 1017–1017. DOI 10.1038/nnano.2017.228.
3. Shlomy I; Divald S; Tadmor K; Leichtmann-Bardoogo Y; Arami A; Maoz BM, ACS Nano 2021. DOI 10.1021/acsnano.0c10141.
4. Niu S; Matsuhisa N; Beker L; Li J; Wang S; Wang J; Jiang Y; Yan X; Yun Y; Burnett W; Poon ASY; Tok JBH; Chen X; Bao Z, Nature Electronics 2019, 2 (8), 361–368. DOI 10.1038/s41928-019-0286-2.
5. Lee S; Franklin S; Hassani FA; Yokota T; Nayeem MOG; Wang Y; Leib R; Cheng G; Franklin DW; Someya T, Science 2020, 370 (6519), 966–970. DOI 10.1126/science.abc9735. [PubMed: 33214278]
6. Fang Y; Zhao X; Tat T; Xiao X; Chen G; Xu J; Chen J, Matter 2021, 4 (4), 1102–1105. DOI 10.1016/j.matt.2021.03.005.
7. Song Y; Mukasa D; Zhang H; Gao W, Accounts of Materials Research 2021, 2 (3), 184–197. DOI 10.1021/accountsmr.1c00002.
8. Ruth SRA; Bao Z, ACS Applied Materials & Interfaces 2020, 12 (52), 58301–58316. DOI 10.1021/acsami.0c19196. [PubMed: 33345539]
9. Ji B; Zhou Q; Wu J; Gao Y; Wen W; Zhou B, ACS Applied Materials & Interfaces 2020, 12 (27), 31021–31035. DOI 10.1021/acsami.0c08910. [PubMed: 32516533]
10. Jeong Y; Gu J; Byun J; Ahn J; Byun J; Kim K; Park J; Ko J; Jeong J.-h.; Amjadi M; Park I, Advanced Healthcare Materials 2021, 10 (9), 2001461. DOI 10.1002/adhm.202001461.
11. Lee J; Woo JY; Kim JT; Lee BY; Han C-S, ACS Applied Materials & Interfaces 2014, 6 (14), 10974–10980. DOI 10.1021/am502639n. [PubMed: 24972024]

12. Zhang Z; Gui X; Hu Q; Yang L; Yang R; Huang B; Yang B-R; Tang Z, Advanced Electronic Materials n/a (n/a), 2100174. DOI 10.1002/aelm.202100174.
13. Yao H; Sun T; Chiam JS; Tan M; Ho KY; Liu Z; Tee BCK, Advanced Functional Materials n/a (n/a), 2008650. DOI 10.1002/adfm.202008650.
14. Ma C; Xu D; Huang Y-C; Wang P; Huang J; Zhou J; Liu W; Li S-T; Huang Y; Duan X, ACS Nano 2020, 14 (10), 12866–12876. DOI 10.1021/acsnano.0c03659. [PubMed: 32938185]
15. Luo Z; Chen J; Zhu Z; Li L; Su Y; Tang W; Omisore OM; Wang L; Li H, ACS Applied Materials & Interfaces 2021, 13 (6), 7635–7649. DOI 10.1021/acsami.0c23042. [PubMed: 33539065]
16. Shi X-X; Chen Y; Jiang H-L; Yu D-L; Guo X-L, Advanced Intelligent Systems n/a (n/a), 2000280. DOI 10.1002/aisy.202000280.
17. Shao Q; Niu Z; Hirtz M; Jiang L; Liu Y; Wang Z; Chen X, Small 2014, 10 (8), 1466–1472. DOI 10.1002/smll.201303601. [PubMed: 24851243]
18. Yoon S; Kim YJ; Lee YR; Lee N-E; Won Y; Gandla S; Kim S; Kim H-K, NPG Asia Materials 2021, 13 (1), 4. DOI 10.1038/s41427-020-00277-6.
19. Chen X; Gao X; Nomoto A; Shi K; Lin M; Hu H; Gu Y; Zhu Y; Wu Z; Chen X; Wang X; Qi B; Zhou S; Ding H; Xu S, Nano Research 2021. DOI 10.1007/s12274-021-3458-0.
20. Jiang Y; Liu Z; Matsuhisa N; Qi D; Leow WR; Yang H; Yu J; Chen G; Liu Y; Wan C; Liu Z; Chen X, Advanced Materials 2018, 30 (12), 1706589. DOI 10.1002/adma.201706589.
21. Wang L; Zhang M; Yang B; Ding X; Tan J; Song S; Nie J, ACS Applied Materials & Interfaces 2021, 13 (4), 5486–5497. DOI 10.1021/acsami.0c18161. [PubMed: 33491443]
22. Zhang Z; Zhang Y; Jiang X; Bukhari H; Zhang Z; Han W; Xie E, Carbon 2019, 155, 71–76. DOI 10.1016/j.carbon.2019.08.018.
23. Chen W; Yan X, Journal of Materials Science & Technology 2020, 43, 175–188. DOI 10.1016/j.jmst.2019.11.010.
24. Ohm Y; Pan C; Ford MJ; Huang X; Liao J; Majidi C, Nature Electronics 2021, 4 (3), 185–192. DOI 10.1038/s41928-021-00545-5.
25. Linghu S; Gu Z; Lu J; Fang W; Yang Z; Yu H; Li Z; Zhu R; Peng J; Zhan Q; Zhuang S; Gu M; Gu F, Nature Communications 2021, 12 (1), 385. DOI 10.1038/s41467-020-20683-2.
26. Shi Y-X; Wu Y; Wang S-Q; Zhao Y-Y; Li T; Yang X-Q; Zhang T, Journal of the American Chemical Society 2021, 143 (10), 4017–4023. DOI 10.1021/jacs.1c00666. [PubMed: 33663217]
27. Wang B; Kostarelos K; Nelson BJ; Zhang L, Advanced Materials 2021, 33 (4), 2002047. DOI 10.1002/adma.202002047.
28. Yin X; Li H; Han L; Meng J; Lu J; Song Q, Small n/a (n/a), 2008056. DOI 10.1002/smll.202008056.
29. Zhang S; Qiu L; Zheng Y; Shi Q; Zhou T; Sencadas V; Xu Y; Zhang S; Zhang L; Zhang C; Zhang C-L; Yu S-H; Guo Z, Advanced Functional Materials 2021, 31 (3), 2006425. DOI 10.1002/adfm.202006425.
30. Xing L; Owusu KA; Liu X; Meng J; Wang K; An Q; Mai L, Nano Energy 2021, 79, 105384. DOI 10.1016/j.nanoen.2020.105384.
31. Jo HS; An S; Park C-W; Woo D-Y; Yarin AL; Yoon SS, ACS Applied Materials & Interfaces 2019, 11 (43), 40232–40242. DOI 10.1021/acsami.9b12847. [PubMed: 31571474]
32. Li D; Chen H; Fan K; Labunov V; Lazarouk S; Yue X; Liu C; Yang X; Dong L; Wang G, Biosensors and Bioelectronics 2021, 181, 113147. DOI 10.1016/j.bios.2021.113147. [PubMed: 33773219]
33. Suwatthanarak T; Thiodorus IA; Tanaka M; Shimada T; Takeshita D; Yasui T; Baba Y; Okochi M, Lab on a Chip 2021, 21 (3), 597–607. DOI 10.1039/D0LC00899K. [PubMed: 33367429]
34. Chen M; Luo W; Xu Z; Zhang X; Xie B; Wang G; Han M, Nature Communications 2019, 10 (1), 4024. DOI 10.1038/s41467-019-12030-x.
35. Han J; Yang J; Gao W; Bai H, Advanced Functional Materials 2021, 31 (16), 2010155. DOI 10.1002/adfm.202010155.
36. Li Z; Chang S; Khuje S; Ren S, ACS Nano 2021. DOI 10.1021/acsnano.1c02209.
37. Wang K; Yap LW; Gong S; Wang R; Wang SJ; Cheng W, Advanced Functional Materials 2021, n/a (n/a), 2008347. DOI 10.1002/adfm.202008347.

38. Wu H; Yang G; Zhu K; Liu S; Guo W; Jiang Z; Li Z, Advanced Science 2021, 8 (2), 2001938. DOI 10.1002/advs.202001938. [PubMed: 33511003]
39. Wang J; Wang J-G; Liu H; You Z; Li Z; Kang F; Wei B, Advanced Functional Materials 2021, 31 (7), 2007397. DOI 10.1002/adfm.202007397.
40. Kim Y; Kim T; Lee J; Choi YS; Moon J; Park SY; Lee TH; Park HK; Lee SA; Kwon MS; Byun H-G; Lee J-H; Lee M-G; Hong BH; Jang HW, Advanced Materials 2021, 33 (2), 2004827. DOI 10.1002/adma.202004827.
41. Han X; Xiao W; Wen S; Lin J; He A; Jiang Q; Nie H, Advanced Electronic Materials 2021, 7 (4), 2001242. DOI 10.1002/aelm.202001242.
42. Huang C-B; Yao Y; Montes-García V; Stoeckel M-A; Von Holst M; Ciesielski A; Samorì P, Small 2021, 17 (8), 2007593. DOI 10.1002/smll.202007593.
43. Li X; Li M; Xu J; You J; Yang Z; Li C, Nature Communications 2019, 10 (1), 3514. DOI 10.1038/s41467-019-11466-5.
44. Wu Z; Yang X; Wu J, ACS Applied Materials & Interfaces 2021, 13 (2), 2128–2144. DOI 10.1021/acsami.0c21841. [PubMed: 33405508]
45. Lee W; Kalashnikov N; Mok S; Halaoui R; Kuzmin E; Putnam AJ; Takayama S; Park M; McCaffrey L; Zhao R; Leask RL; Moraes C, Nature Communications 2019, 10 (1), 144. DOI 10.1038/s41467-018-07967-4.
46. Ma Z; Huang Q; Xu Q; Zhuang Q; Zhao X; Yang Y; Qiu H; Yang Z; Wang C; Chai Y; Zheng Z, Nature Materials 2021. DOI 10.1038/s41563-020-00902-3.
47. Jang J; Kim J; Shin H; Park Y-G; Joo BJ; Seo H; Won J.-e.; Kim DW; Lee CY; Kim HK; Park J-U, Science Advances 2021, 7 (14), eabf7194. DOI 10.1126/sciadv.abf7194. [PubMed: 33789904]
48. Qiao Y; Wang Y; Jian J; Li M; Jiang G; Li X; Deng G; Ji S; Wei Y; Pang Y; Wu Q; Tian H; Yang Y; Wu X; Ren T-L, Carbon 2020, 156, 253–260. DOI 10.1016/j.carbon.2019.08.032.
49. Jiang Y; Dong K; Li X; An J; Wu D; Peng X; Yi J; Ning C; Cheng R; Yu P; Wang ZL, Advanced Functional Materials 2021, 31 (1), 2005584. DOI 10.1002/adfm.202005584.
50. Guo Z; Sun C; Zhao J; Cai Z; Ge F, Advanced Materials Interfaces 2021, 8 (3), 2001695. DOI 10.1002/admi.202001695.
51. Liu Q; Tian B; Liang J; Wu W, Materials Horizons 2021. DOI 10.1039/D0MH01950J.
52. Tang L; Shang J; Jiang X, Science Advances 2021, 7 (3), eabe3778. DOI 10.1126/sciadv.abe3778. [PubMed: 33523888]
53. Patel M; Seo JH; Kim S; Nguyen TT; Kumar M; Yun J; Kim J, Journal of Power Sources 2021, 491, 229578. DOI 10.1016/j.jpowsour.2021.229578.
54. Huang S; Liu Y; Jafari M; Siaj M; Wang H; Xiao S; Ma D, Advanced Functional Materials 2021, 31 (14), 2010022. DOI 10.1002/adfm.202010022.
55. Huang S; Zhang Q; Yang F; Gangadharan DT; Li P; Ren F; Sun B; Ma D, Journal of Materials Chemistry A 2020, 8 (17), 8620–8628. DOI 10.1039/C9TA14030A.
56. Yu S; Liu X; Wu M; Dong H; Wang X; Li L, ACS Applied Materials & Interfaces 2021, 13 (12), 14470–14478. DOI 10.1021/acsami.0c22324. [PubMed: 33733722]
57. Lee S; Jang J; Park T; Park YM; Park JS; Kim Y-K; Lee H-K; Jeon E-C; Lee D-K; Ahn B; Chung C-H, ACS Applied Materials & Interfaces 2020, 12 (5), 6169–6175. DOI 10.1021/acsami.9b17168. [PubMed: 31933356]
58. Lu X; Zhang Y; Zheng Z, Advanced Electronic Materials 2021, n/a (n/a), 2001121. DOI 10.1002/aelm.202001121.
59. Patil JJ; Chae WH; Trebach A; Carter K-J; Lee E; Sannicolo T; Grossman JC, Advanced Materials 2021, 33 (5), 2004356. DOI 10.1002/adma.202004356.
60. Dou L; Cui F; Yu Y; Khanarian G; Eaton SW; Yang Q; Resasco J; Schildknecht C; Schierle-Arndt K; Yang P, ACS Nano 2016, 10 (2), 2600–2606. DOI 10.1021/acsnano.5b07651. [PubMed: 26820809]
61. Pang Y; Zhang K; Yang Z; Jiang S; Ju Z; Li Y; Wang X; Wang D; Jian M; Zhang Y; Liang R; Tian H; Yang Y; Ren TL, ACS Nano 2018, 12 (3), 2346–2354. DOI 10.1021/acsnano.7b07613. [PubMed: 29378401]

62. Muhammad Hafiz S; Ritikos R; Whitcher TJ; Razib N Md.; Bien DCS; Chanlek N; Nakajima H; Saisopa T; Songsiriritthigul P; Huang NM; Rahman SA, Sensors and Actuators B: Chemical 2014, 193, 692–700. DOI 10.1016/j.snb.2013.12.017.
63. Johra FT; Lee J-W; Jung W-G, Journal of Industrial and Engineering Chemistry 2014, 20 (5), 2883–2887. DOI 10.1016/j.jiec.2013.11.022.
64. Mazur M; Kaczmarek D; Domaradzki J; Wojcieszak D; Song S; Placido F In Influence of thickness on transparency and sheet resistance of ITO thin films, The Eighth International Conference on Advanced Semiconductor Devices and Microsystems, 25-27 Oct. 2010; 2010; pp 65–68.
65. Hecht DS; Thomas D; Hu L; Ladous C; Lam T; Park Y; Irvin G; Drzaic P, Journal of the Society for Information Display 2009, 17 (11), 941–946. DOI 10.1889/JSID17.11.941.
66. Zhang X; Wu J; Wang J; Zhang J; Yang Q; Fu Y; Xie Z, Solar Energy Materials and Solar Cells 2016, 144, 143–149. DOI 10.1016/j.solmat.2015.08.039.
67. Ye S; Rathmell AR; Stewart IE; Ha Y-C; Wilson AR; Chen Z; Wiley BJ, Chemical Communications 2014, 50 (20), 2562–2564. DOI 10.1039/C3CC48561G. [PubMed: 24346590]
68. Zhu Y; Kim S; Ma X; Byrley P; Yu N; Liu Q; Sun X; Xu D; Peng S; Hartel MC; Zhang S; Jucaud V; Dokmeci MR; Khademhosseini A; Yan R, Nano Research 2021. DOI 10.1007/s12274-021-3718-z.
69. Liu Q; Kim S; Ma X; Yu N; Zhu Y; Deng S; Yan R; Zhao H; Liu M, Nanoscale 2019, 11 (16), 7790–7797. DOI 10.1039/C8NR08983C. [PubMed: 30951064]
70. Mehta R; Chugh S; Chen Z, Nano Letters 2015, 15 (3), 2024–2030. DOI 10.1021/nl504889t. [PubMed: 25650635]
71. Garnett EC; Cai W; Cha JJ; Mahmood F; Connor ST; Greyson Christoforo M; Cui Y; McGehee MD; Brongersma ML, Nature Materials 2012, 11 (3), 241–249. DOI 10.1038/nmat3238. [PubMed: 22306769]
72. Lee P; Lee J; Lee H; Yeo J; Hong S; Nam KH; Lee D; Lee SS; Ko SH, Advanced materials 2012, 24 (25), 3326–3332. [PubMed: 22610599]
73. Cui F; Yu Y; Dou L; Sun J; Yang Q; Schildknecht C; Schierle-Arndt K; Yang P, Nano Letters 2015, 15 (11), 7610–7615. DOI 10.1021/acs.nanolett.5b03422. [PubMed: 26496181]
74. Ye S; Rathmell AR; Chen Z; Stewart IE; Wiley BJ, Advanced Materials 2014, 26 (39), 6670–6687. DOI 10.1002/adma.201402710. [PubMed: 25252266]
75. Huang Y; Wang Y; Sun X; Guo X; Zhang Y; Wang Z; Liu P; Liu C; Qiu J; Zhang Y, Smart Materials and Structures 2020, 29 (4), 045014. DOI 10.1088/1361-665x/ab73e1.
76. Qiu J; Guo X; Chu R; Wang S; Zeng W; Qu L; Zhao Y; Yan F; Xing G, ACS Applied Materials & Interfaces 2019, 11 (43), 40716–40725. DOI 10.1021/acsami.9b16511. [PubMed: 31596567]
77. Wang X; Meng X; Zhu Y; Ling H; Chen Y; Li Z; Hartel MC; Dokmeci MR; Zhang S; Khademhosseini A, IEEE Electron Device Letters 2021, 42 (1), 46–49. DOI 10.1109/LED.2020.3042310. [PubMed: 33746352]
78. Gong S; Schwalb W; Wang Y; Chen Y; Tang Y; Si J; Shirinzadeh B; Cheng W, Nature Communications 2014, 5 (1), 3132. DOI 10.1038/ncomms4132.
79. Tai Y; Mulle M; Aguilar Ventura I; Lubineau G, Nanoscale 2015, 7 (35), 14766–14773. DOI 10.1039/C5NR03155A. [PubMed: 26288336]
80. Ge G; Zhang Y; Shao J; Wang W; Si W; Huang W; Dong X, Advanced Functional Materials 2018, 28 (32), 1802576. DOI 10.1002/adfm.201802576.
81. Zhu Y; Cai H; Ding H; Pan N; Wang X, ACS Applied Materials & Interfaces 2019, 11 (6), 6195–6200. DOI 10.1021/acsami.8b17085. [PubMed: 30666869]
82. Wu Q; Qiao Y; Guo R; Naveed S; Hirtz T; Li X; Fu Y; Wei Y; Deng G; Yang Y; Wu X; Ren T-L, ACS Nano 2020, 14 (8), 10104–10114. DOI 10.1021/acsnano.0c03294. [PubMed: 32667779]
83. Adji A; Hirata K; O'Rourke MF, Blood Pressure Monitoring 2006, 11 (4).
84. Hu L; Kim HS; Lee J-Y; Peumans P; Cui Y, ACS Nano 2010, 4 (5), 2955–2963. DOI 10.1021/nn1005232. [PubMed: 20426409]

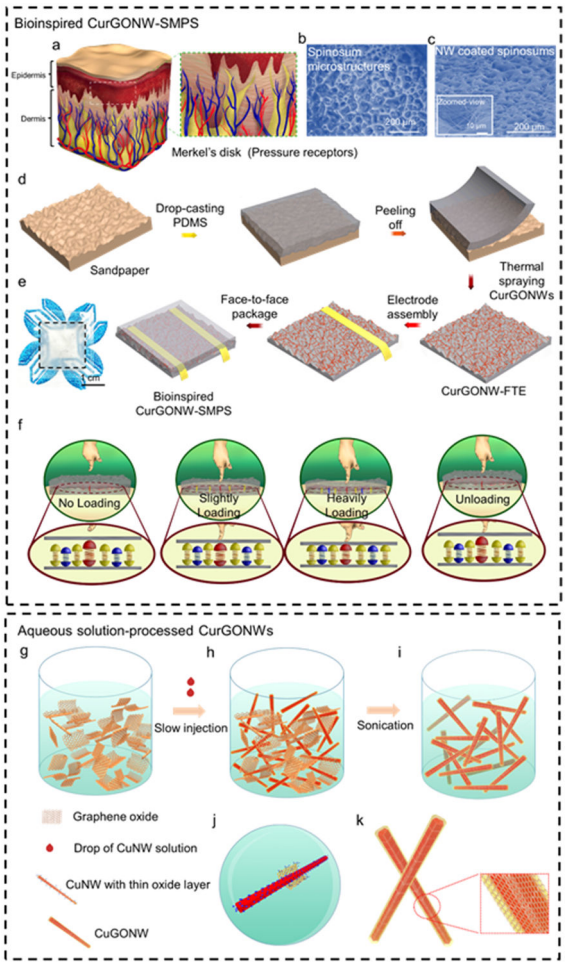

Figure 1. Schematics of the epidermis-bioinspired CurGONW-SMPS.

Bioinspired CurGONW-SMPS. (a) Illustration displaying the biological microstructure of the epidermis and the micro-spined layer is an essential element for high sensitivity. (b) Microscopy of the sandpaper demonstrates a similar topography as the epidermis. (c) SEM image and its magnified view of bioinspired spinosum microstructured piezoresistive sensor with CurGONWs. (d) The fabrication process of bioinspired spinosum microstructured piezoresistive sensor with CurGONWs. More fabrication details could be found in experimental section 4. (e) Photographs of the resulted bioinspired piezoresistive sensor device. (f) Mechanism revelation of the bioinspired spinosum microstructured piezoresistive sensor with CurGONWs in the pristine state under preloading, slightly loading, heavily loading, and unloading conditions. Aqueous solution-processed CurGONWs. (g) GO nanosheet aqueous solution was homogeneously dispersed into methanol solution. (h) CuNW toluene solution was added to this diluted GO solution with stirring. (i) The mixture was sonicated for several minutes to form the CuGONW. (j) The magnified view of graphene oxide nanosheets coated on CuNW surface during sonication. (k) The magnified image of CuGONWs.

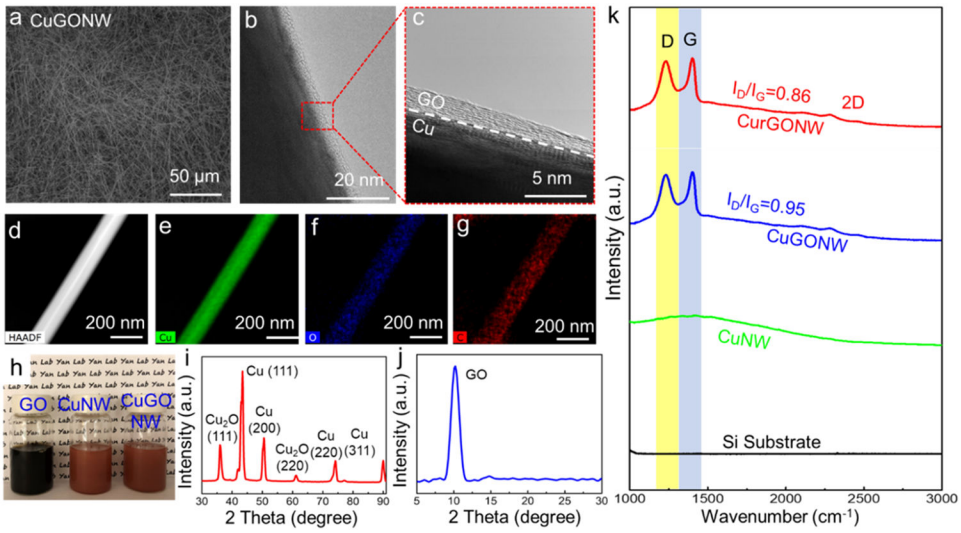

Figure 2. Structure characterizations of the CuGONWs.

(a) Low magnification SEM image of CuGONW samples. (b, c) TEM image and its magnified view of CuGONW confirm that the GO layer is conformal and uniformly coated on CuNW surfaces. (d-g) EDS characterization of represented CuGONW revealing the elemental distribution of copper, oxygen, and carbon that further confirms its core-shell architecture. (h) Digital image of GO nanosheet solution, pristine CuNWs, and the as-synthesized CuGONWs. (i-j) XRD measurement of CuGONWs. (k) Raman spectra of CurGONWs, CuGONWs, CuNWs, and Si substrate under a wavelength of 532 nm, displaying showing the distinct GO/rGO peaks on CuGONW or CurGONW samples, while no similar peaks are seen on CuNW and the silicon substrate. Cu fluorescence background could also be detected in samples containing CuNW. I_D/I_G decreased after the CuGONW sample was annealed in forming gas under 280 °C for one hour, suggesting a significant recovery of the conjugated graphitic framework after de-functionalizing oxygen functional groups, which means the GO layer was thermally reduced to rGO.

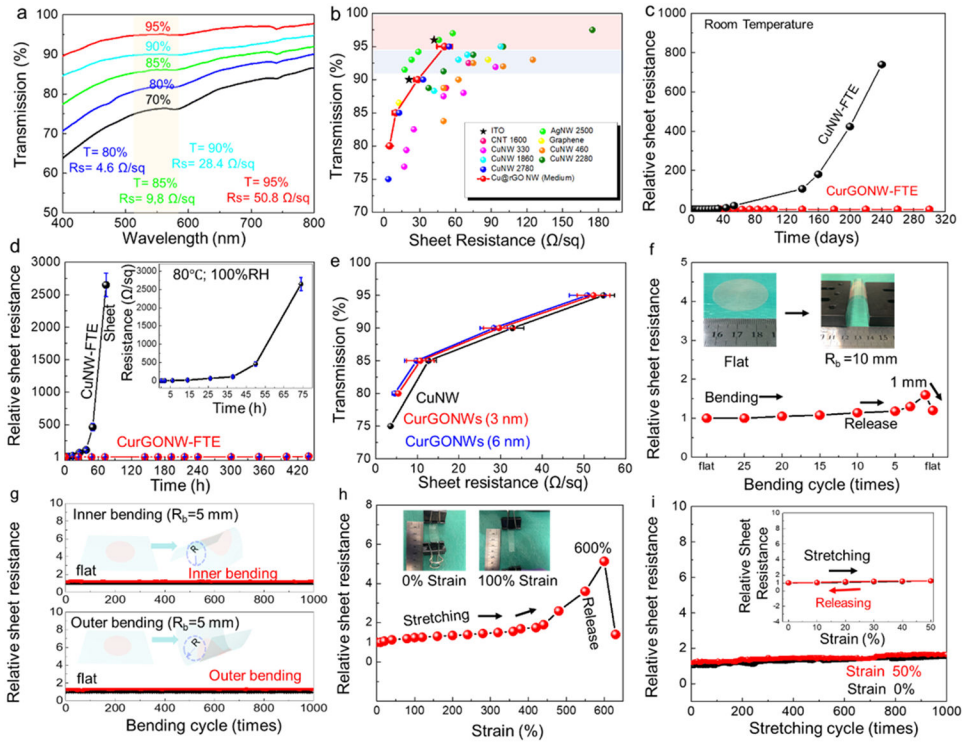

Figure 3. CurGONW-FTEs and their optical and electrical performance with long-term stability.

(a) Wavelength-dependent transmittance and corresponding sheet resistance of the electrodes. (b) A plot of optical transmittance vs. sheet resistance of CurGONW-FTEs (red line with symbol). For comparison, published data of the current state-of-the-art transparent electrodes, including ITO[64], CNT[65], PEDOT,[66] AgNWs,[67] and CuNWs, [67] were also plotted. (c) Long-term stability of CurGONW- and CuNW-FTEs under ambient conditions. (d) Long-term stability of CurGONW- and CuNW-FTEs under a high temperature (80 °C) and humidity (100%) condition. (e) Optical/electrical performance of the CurGONW-FTEs with different rGO coating thicknesses. (f) Conductivity change of CurGONW-FTEs when bending to a 5 mm-bending radius (Inner and outer bending) and then strengthening each cycle. The conductivity becomes stable after several cycles. The inset shows the bending process. (g) Conductivity variation of the CurGONW-FTEs at a bending radius up to 1 mm in the first cycle. The inset displays the flat and bent electrode (PET as a substrate). (h) Conductivity changes of the CurGONW-FTEs (PDMS as a substrate) after multiple 50% stretching-cycles. The FTE was slowly stretched to a strain of 50% and then released to 0% strain under the constant stretching rate in each cycle. The inset depicts the resistance change of the FTE in a representative stretch/release cycle. (i) Conductivity variation of the electrode as a response of tensile strain until fracture. The inset displays the single stretching-releasing cycle. Multiple CurGONW-FTEs were tested, and the conductivity performance shows good reliability under the constant mechanical deformation. The transmittance in this electrode is 80% for all the electrodes. R_0 refers to the sheet resistance of the pristine electrode.

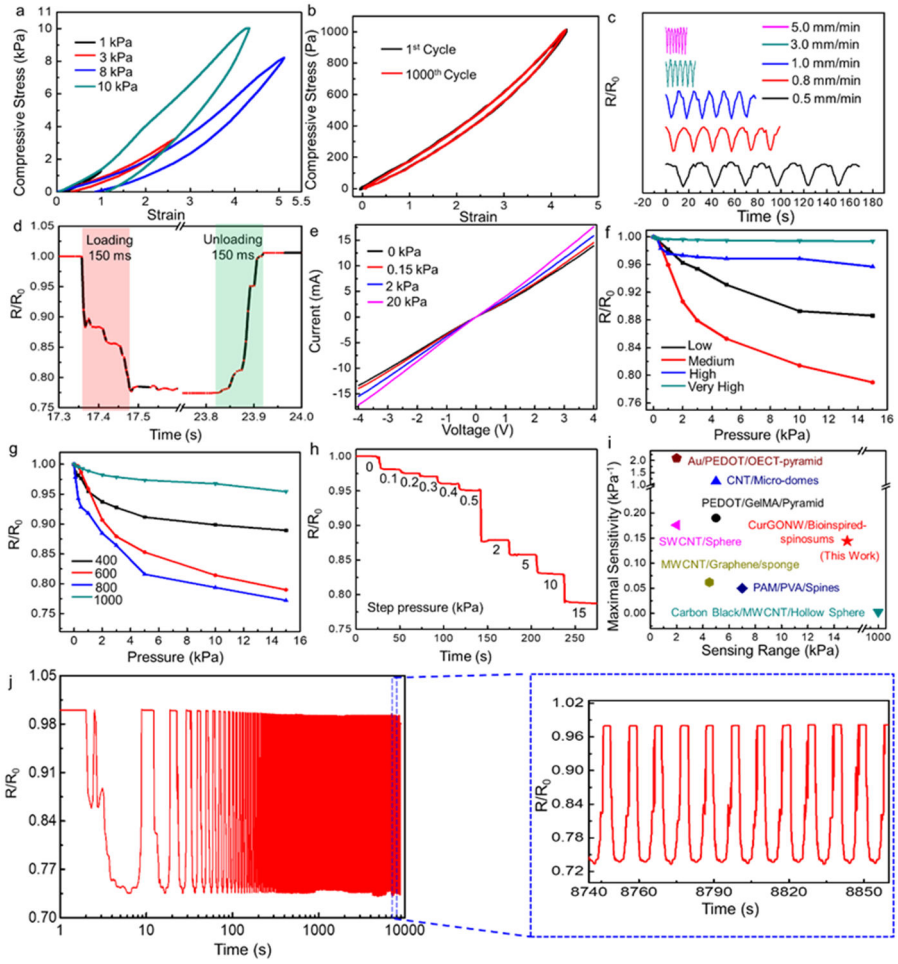

Figure 4. Mechanical and electrical characterization of the epidermis-bioinspired CurGONW-SMPS.

(a) Stress-strain curves of the CurGONW-SMPS for cyclic elastic recovery tests under various compression stress. (b) Stress-strain of the bioinspired CurGONW-SMPS under 1 kPa for the 1st and 1000th cycle. (c) The change in resistance under different compression rates with an applied pressure of 1 kPa. (d) Response time of the bioinspired CurGONW-SMPS. (e) The *I-V* curves of epidermis-bioinspired CurGONW-SMPS are made with the 800-grit sandpaper template. The linear correlation of voltage on current under varied pressures confirms the ohmic relationship between CurGONWs and spinosum microstructured substrate. (f) Sensitivity of the bioinspired piezoresistive sensor with varying loadings of CurGONWs (low, medium, high, very high). The one coated with a medium concentration of CurGONWs displayed a maximal sensitivity. (g) Sensitivity comparison of the bioinspired sensors fabricated using different surface roughness (400, 600, 800, and 1000). The sensor made with sandpaper no. 800 exhibits the highest sensitivity compared with those made with other roughness. (h) The representative resistance change for a step pressure from 0 to 15 kPa (from sandpaper no. 800). (i) Comparison of maximum sensitivity vs. maximum range with other published data[75-80]. (j) Cycling test of the bioinspired CurGONW-SMPS for around 1000 cycles at a constant

pressure of 15 kPa. It confirms the excellent stability and durability of the bioinspired CurGONW-SMPS.

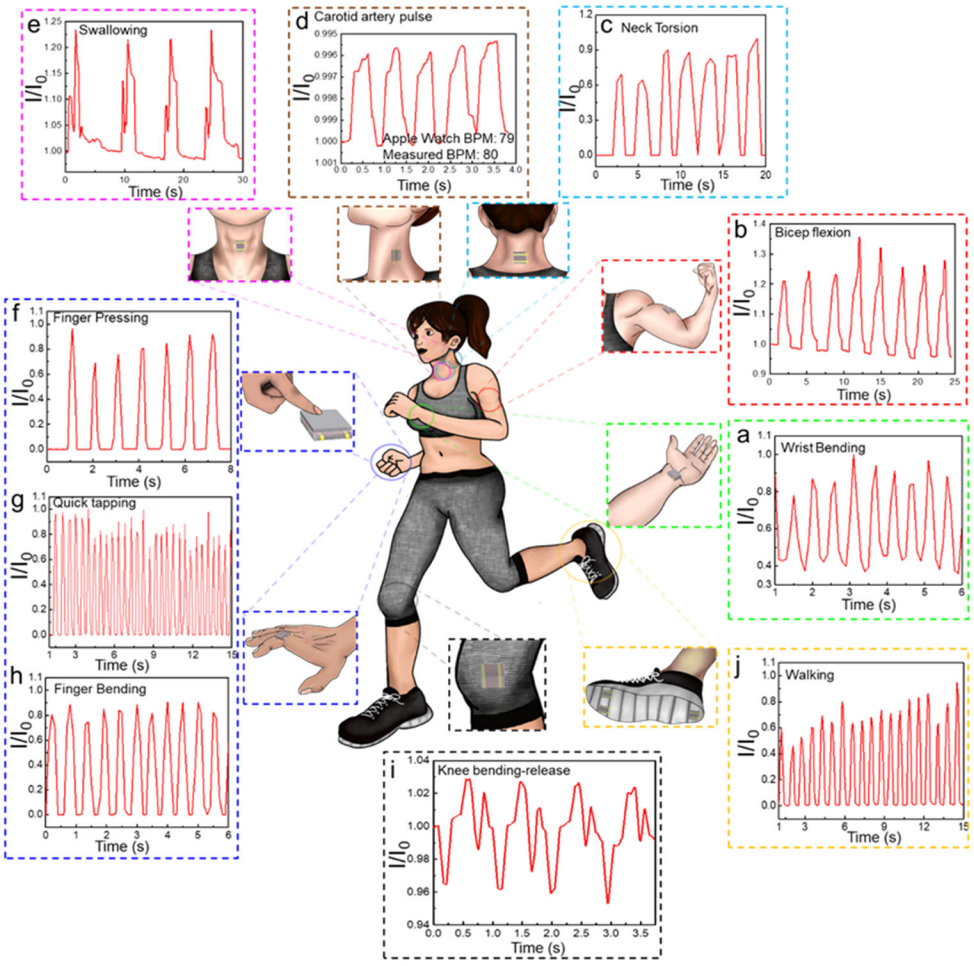

Figure 5. Wearable applications of the epidermis-bioinspired CurGONW-SMPS for real-time monitoring of human motions and subtle physiological signals.

The signal feedback in the form of current change comes from (a) wrist bending, (b) bicep flexion, (c) neck torsion, (d) carotid artery pulse, (e) throat swallowing, (f) finger pressing, (g) quick tapping, (h) finger bending, (i) knee bending-release cycle, and (j) walking.